

Entangled photon pair excitation and time-frequency filtered multidimensional photon correlation spectroscopy as a probe for dissipative exciton kinetics

Arunangshu Debnath^{1,*} and Shaul Mukamel^{2,†}

¹*Center for Free-Electron Laser Science CFEL, Deutsches Elektronen-Synchrotron DESY, Notkestrasse 85, 22607 Hamburg, Germany*

²*Department of Chemistry and Department of Physics and Astronomy, University of California, Irvine, California 92697, USA*

In molecular aggregates, multiple delocalized exciton states interact with phonons, making the state-resolved spectroscopic monitoring of dynamics challenging. We propose a protocol that combines photon-entanglement-enhanced narrowband excitation of two-exciton states with time-frequency-filtered two-photon coincidence counting. It can alleviate bottlenecks associated with probing exciton dynamics spread across multiple spectral and temporal windows. We demonstrate that non-classical correlations of entangled photon pairs can be used to prepare narrowband two-exciton population distributions, circumventing transport in mediating states. The distributions thus created can be monitored using time-frequency-filtered photon coincidence counting, and the pathways contributing to photon emission events can be classified by tuning filtering parameters. Numerical simulations for a light-harvesting aggregate highlight the ability of this protocol to achieve selectivity by suppressing or amplifying specific pathways. Combining entangled photonic sources and multidimensional photon counting allow promising applications to spectroscopy and sensing.

I. INTRODUCTION

In photosynthetic systems, light-harvesting complexes are critical components that facilitate efficient photon energy conversion through exciton formation and transport. Investigating the structural and functional mechanisms of exciton dynamics provides essential insights for engineering biomimetic energy-harvesting systems. In these systems, aggregated chromophores serve as the energy harvesters. The aggregation of individual chromophores results in delocalized electronic excitations: molecular excitons which are primarily of the Frenkel type. The excitons, often generated through photo-excitation, participate in multiscale relaxation and dephasing kinetics, due to the interaction with phonons [1–3], ultimately leading to the primary charge separation processes. Previous investigations have sought to monitor the role of coherent energy transfer that results from transition dipole-dipole interactions. The latter can be probed via multi-pulse four-wave mixing techniques, popularly known as two-dimensional spectroscopy. The investigation multi-exciton states, where signatures of exciton-exciton correlations can be found, have comparatively received less attention. The early attributes of such correlations can already be seen in the two-exciton state energetics. Prior investigations have demonstrated that various modalities of two-photon absorption spectroscopy, resonant and off-resonant, can spectroscopically monitor these resonances [4–20]. Probing state-resolved dynamics in the two-exciton manifolds is complicated by the high density of states that take part in phonon-induced dissipation spanning multiple time and energy scales. Over the past

several years, a series of proposals, limited to atomic, and simple molecular systems have underscored the advantages of employing entangled photon sources to improve accessibility of doubly excited states while scaling favorably with the probe intensity [21–35]. These proposals were complemented by examinations of the role of photon entanglement in the context of the reported enhancements [36–43]. Parallel theoretical investigations have established that exploiting the non-classical time-frequency correlations of photonic states may yield superior signal resolution in spectroscopic measurements compared to classical counterparts [27, 44].

To monitor the fate of two-exciton states, multiphoton fluorescence intensity correlation measurements have been proposed [35, 45–48]. In a series of work [47, 48], the concept of multidimensional signal measurements was extended to include coincidence counting measurements. This theoretical framework promises to transparently link information derived from photon correlation measurements to molecular events. The time and frequency filtered n -photon coincidence counting measurements provide a $2n$ -dimensional parameter space for the events to be classified. However to firmly establish their role as a routine spectroscopic tool in extended molecular systems, it requires a protocol combining them with efficient initial state preparation strategies.

The two-exciton states in molecular aggregates, such as light-harvesting complexes, are typically prepared via the manifold of one-exciton states, which are subject to phonon-induced transport and dephasing. Furthermore, as the number of chromophoric sites increases, the number of one-exciton and two-exciton states increases as well. As a consequence, the number of interfering optical transitions may increase dramatically. Additionally, phonon-induced transport redistributes the population among the participating states during the dynamics. In this work, we demonstrate that state-selective entan-

* arunangshu.debnath@desy.de

† smukamel@uci.edu

gled photon excitation and time-frequency-filtered multidimensional correlation spectroscopy can serve as an efficient probe for dissipative exciton kinetics. Specifically, this approach helps unravel two-exciton transport kinetics by monitoring cascaded photon emission events, tracking the correlation between these events, and benchmarking the nature of the exciton wavepacket created by entangled photon excitation.

We focus on the light-harvesting complex LHCII, the most abundant antenna complex in plants and an important constituent of Photosystem II. It exists as a trimeric structure composed of structurally rigid monomeric aggregates; each monomer contains of several chlorophylls whose lowest energy levels are spectroscopically accessible. Exciton dynamics in LHCII exhibit significant complexity, particularly regarding the behavior of higher-order excitations. The combined protocol is shown to provide mechanistic insight into the cooperative exciton kinetics of LHCII, even in the presence of spectral weight redistribution caused by mode mixing and relaxation. In the following, in section II, we introduce the exciton-phonon Hamiltonian of the light-harvesting complex LHCII, which serves as our test system, and the photonic sources. This is complemented by the Appendix A. In the subsequent three subsections of Sec. III (III A–III C), we detail the theoretical framework and numerical simulations of the combined protocol. The manuscript concludes in Sec. IV with a summary of our findings, a discussion of future outlook, and a brief examination of the current limitations.

II. DRIVEN DISSIPATIVE ONE- AND TWO-EXCITON KINETICS

The dissipative one- and two-exciton dynamics of the light-harvesting complex LHCII are simulated using the Frenkel exciton model within the Heitler-London approximation. The model is constructed by considering the lowest three electronic energy states of each of the chlorophyll molecules. The Hamiltonian (with $\hbar = 1$) is given by,

$$\begin{aligned} H = & \sum_{mn} (E_m \delta_{mn} + J_{mn}) B_m^\dagger B_n \\ & + \sum_{mn} U_m^{(1)} B_m^\dagger B_m B_m^\dagger B_m + U_{mn}^{(2)} B_m^\dagger B_n^\dagger B_n B_m \\ & + \sum_j \omega_j (b_j^\dagger b_j + \frac{1}{2}) + \sum_{m,j} g_{m,j} (b_j^\dagger + b_j) B_m^\dagger B_m \end{aligned} \quad (1)$$

Here, the on-site excitation energy, E_m , and inter-site hopping, J_{mn} , are accounted for by the first term in the Hamiltonian. The Coulomb interaction, responsible for the inter-site hopping, results in the delocalization of the exciton states across the sites. The higher-order excitonic nonlinearities that shift exciton energy states are given by $U_m^{(1)}$ and $U_{mn}^{(2)}$. The exciton creation (annihilation) operators, B_m^\dagger (B_m), follow the commutation re-

lation $[B_n, B_m^\dagger] = \delta_{mn}(1 - \eta(B_m^\dagger B_m)^2)$, where $\eta = 3/2$, while the phonon creation (annihilation) operators, b_j^\dagger (b_j), follow $[b_i, b_j^\dagger] = \delta_{ij}$. The two-exciton Hamiltonian can be constructed as $H_{mnkl}^{(2)} = H_{mn}^{(1)} \delta_{kl} + \delta_{mn} H_{kl}^{(1)}$, where $H_{mn}^{(1)}$ is given by the first line of the Eq. 1. For the LHCII, the number of chromophoric sites is $N_s = 14$, which yields $N_g = 1$ ground state, $N_e = 14$ one-exciton states, and $N_f = 105$ two-exciton states, composed of 14 overtone and 91 combination states. The excitonic eigenstates are obtained by the exact diagonalization of the exciton-number conserving Hamiltonian blocks as:

$$\begin{aligned} |e_j\rangle &= \sum_m T_{j,m}^{(1)} B_m^\dagger |0\rangle \\ |f_k\rangle &= \sum_{mn} T_{k,mn}^{(2)} B_m^\dagger B_n^\dagger |0\rangle \end{aligned} \quad (2)$$

These transformation coefficients, $T^{(n)}$ (for the n –th manifold) define the spectral weights associated with the delocalized eigenstates. It is noteworthy that the energies of the two-exciton overtone and combination states, dependent on the nonlinearity terms $U_m^{(1)}$ and $U_{mn}^{(2)}$ respectively, deviate from the sum of two one-exciton states. As a consequence, the relative ordering of states within the two-exciton manifold is contingent upon two competing sets of parameters, governing exciton delocalization and localization. The latter influence, via excited state absorption processes, all three pathways responsible for the two-photon absorption events addressed in this article. The Green's functions (valid for both one and two exciton manifold) describing can be represented in a compact form as follows

$$\begin{aligned} \mathcal{G}_{a_1 a_2, a_3 a_4}(t) = & \delta_{a_1 a_2} \delta_{a_3 a_4} \theta(t) [\exp(-Kt)]_{a_1 a_1, a_3 a_3} \\ & + (1 - \delta_{a_1 a_2}) \delta_{a_1 a_3} \delta_{a_2 a_4} \theta(t) \exp(-i\omega_{a_1 a_3} t - \gamma_{a_1 a_3} t) \end{aligned} \quad (3)$$

The optical properties of exciton aggregates consisting of multiple three level emitters are primarily dictated by the nature of intermolecular interactions and two-exciton nonlinearities [2, 13, 49]. The interaction with photonic sources, within the rotating wave approximation, can be described by the following Hamiltonian

$$\begin{aligned} H_{\text{int}}(t) = & EV^\dagger + E^\dagger V = \sum_{j,pq \in \{ge,ef\}} \sqrt{\frac{2\pi\omega_j}{V}} \\ & \left(a_j \exp(-i\omega_j t) \exp(i\omega_{pq} t) B_{pq} + \text{h.c.} \right) \end{aligned} \quad (4)$$

where $B_{pq}(t) = d_{pq} |p\rangle \langle q|$ (with properties $\{p,q\} \in g, e, f$, and a_j are the exciton and photon annihilation operators, describing inter-manifold exciton transition and excitations in the photonic modes, respectively. For our case, the deployed photonic sources are entangled photon pairs generated via spontaneous parametric down-conversion (SPDC) in the weak-down-conversion limit. In a typical scenario, a birefringent crystal is pumped

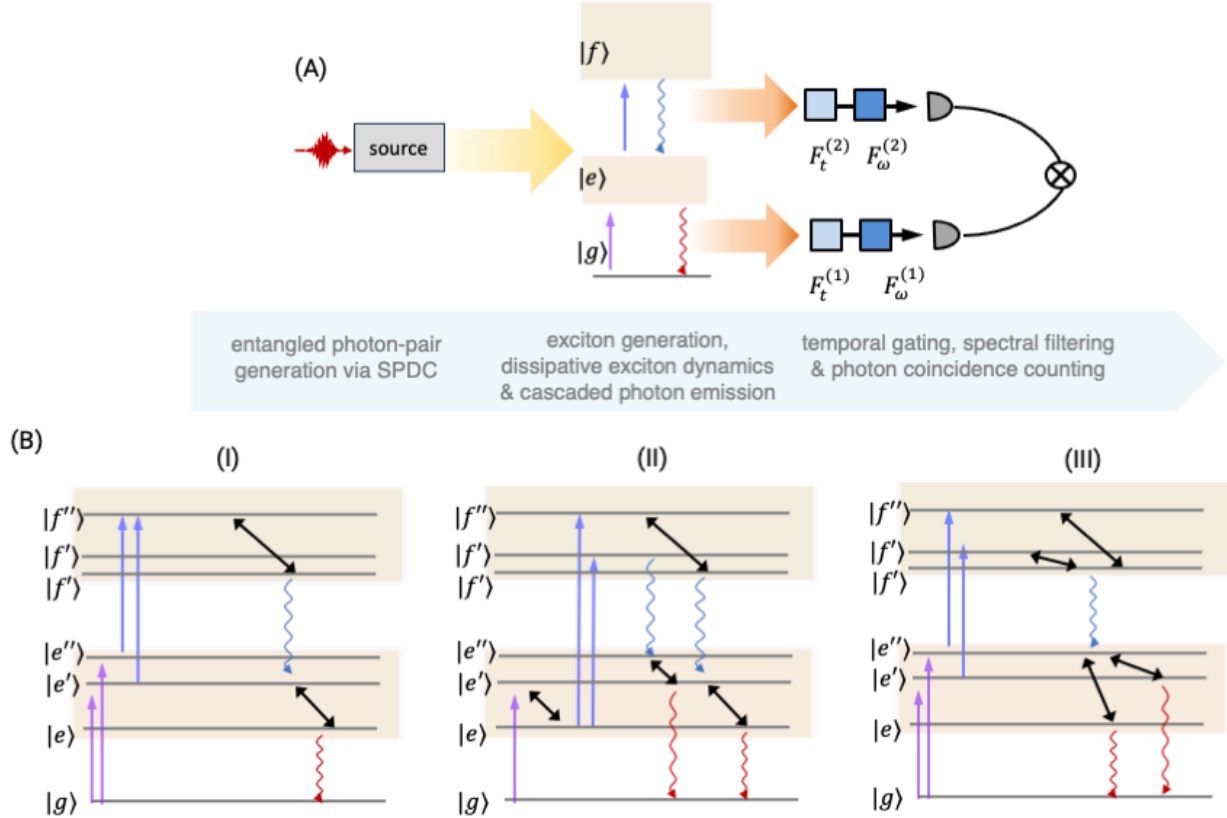


FIG. 1: (A) Illustration of the proposed protocol, consisting of the driving, evolution, and detection stages. The process is assisted by entangled photon pairs and temporal-spectral filtering of emitted photons. In (B), three plausible snapshots of the dynamics (I)-(III), featuring increasingly complex pathways, that may be monitored using the protocol is displayed. In the simulation, the exciton transport within both manifolds is accounted for. Since these pathways may be simultaneously present in the dynamics, the protocol allows for selective probing and aids in constructing a mechanistic narrative.

with a classical pump that precedes to the generation of correlated photon pairs with frequencies ω_s, ω_i . It involves two field-matter interactions with the incoming classical field modes and four interactions with the outgoing signal-idler fields. The correlation properties of the emitted photon field is determined by the physical properties of the SPDC crystal [21–23, 27, 50–52]. The incoming entangled photon states can be described by the two photon state of the photon field

$$\rho_{\text{photon}} = \int \frac{d\omega_1}{2\pi} \int \frac{d\omega_2}{2\pi} \int \frac{d\omega'_1}{2\pi} \int \frac{d\omega'_2}{2\pi} F(\omega_1, \omega_2) F^*(\omega'_1, \omega'_2) a_{\omega_1}^\dagger a_{\omega_2}^\dagger |0\rangle \langle 0| a_{\omega'_1} a_{\omega'_2} \quad (5)$$

The entangled photon field correlation function is obtained as,

$$\langle E^\dagger(\omega'_b) E^\dagger(\omega'_a) E(\omega_b) E(\omega_b) \rangle = F^*(\omega'_b, \omega'_a) F(\omega_a, \omega_b) \quad (6)$$

where,

$$F(\omega_a, \omega_b) = \alpha A_p(\omega_p) \left\{ \text{sinc}[\phi(\omega_a, \omega_b)] \exp(i\phi(\omega_a, \omega_b)) + \omega_1 \leftrightarrow \omega_2 \right\} \text{with} \\ \phi(\omega_a, \omega_b) = (\omega_a - \omega_1) \tilde{T}_1/2 + (\omega_b - \omega_1) \tilde{T}_2/2 \quad (7)$$

where α governs the down-conversion efficiency. The temporal entanglement parameter of the photon pair sources is given by $\tilde{T}_{\text{ent}} = \tilde{T}_2 - \tilde{T}_1$ establish the upper bound for the interaction time interval. The transform-limited field profile of the SPDC pump, $A_p(\omega_a, \omega_b)$ is taken as a Gaussian, given by, $A_p(\omega_a, \omega_b) = E_0 \sqrt{\pi/\Gamma_{p,0}} \exp[-(\omega - \omega_a - \omega_b)^2/4\Gamma_{p,0}]$, where $\Gamma_{p,0}$ is the temporal width. The quantity is dependent on the time delays acquired by the signal and idler photons during the propagation within the nonlinear crystal. In contrast to entangled photon pairs, the correlation function of coherent laser fields would have factorized into the

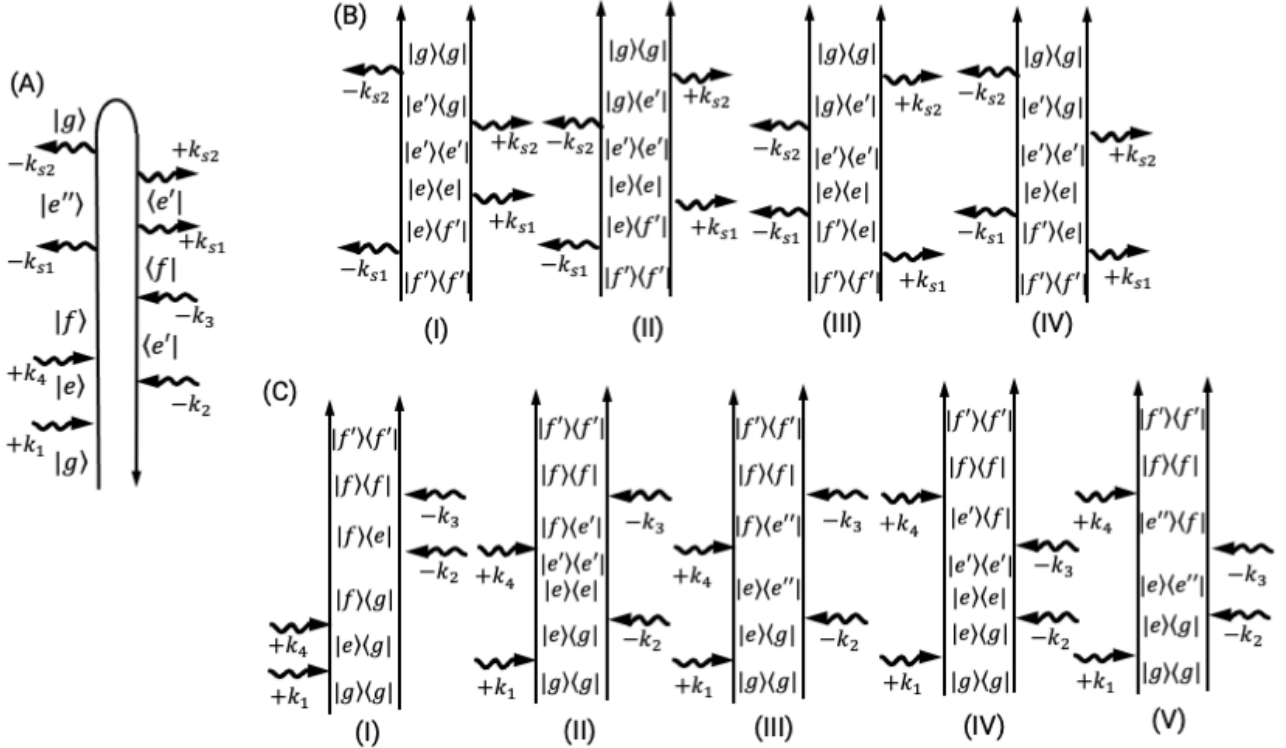


FIG. 2: (A) Diagrammatic illustration (using the Schwinger-Keldysh loop representation) of the pathways involved in the proposed protocol, consisting of the driving, evolution, and emission stages. (B)-(C) Diagrammatic illustration (using the Liouville superoperator representation, suitable for dissipative systems) of the pathways involved in filtered emission (B) and excitation (C). The combinatorial pairing of five possible excitation diagrams and four possible emission diagrams gives rise to all possible pathways that contribute to the final signal. The corresponding key equations are presented in Section III.

product of four amplitude functions, i.e.

$$\begin{aligned} & \langle E^\dagger(\omega_4)E^\dagger(\omega_3)E(\omega_2)E(\omega_1) \rangle \\ &= A_4^*(\omega_4)A_3^*(\omega_3)A_1(\omega_2)A_1(\omega_1) \end{aligned} \quad (8)$$

and the signal would have scaled with the square of the incoming field intensity.

III. RESULTS

The excitation-evolution-emission events occur in three stages. Excitation by entangled photon pairs

creates a tailored two-exciton wavepacket. The two-exciton wavepacket or density operator populations undergo transport, leading to a redistribution of populations over a finite waiting time. This redistributed population serves as the initial configuration for photon emission events. The cascaded two-photon emission process proceeds via two one-photon emissions interleaved by exciton transport in the one-exciton manifold. The signal can be expressed in a compact superoperator form

$$S(\bar{t}_s, \bar{\omega}_s; \bar{t}_i, \bar{\omega}_i) = \int_{-\infty}^{\infty} dt'_s d\tau_s \int_{-\infty}^{\infty} dt'_i d\tau_i \sum_{s,s',i,i'} \text{Tr}_{s,s',i,i'} [D^{(s,s')}(t'_s, \bar{\omega}_s; t'_s, \tau_s) D^{(i,i')}(t'_i, \bar{\omega}_i; t'_i, \tau_i) B^{(s,s',i,i')}(t'_s, \tau_s; t'_i, \tau_i)] \quad (9)$$

where the superoperator for filtered detection

$$\begin{aligned} & D^{(\nu,\nu')}(t_\nu, \bar{\omega}_\nu; t'_\nu, \tau_\nu) \\ &= D(\bar{t}_\nu, \bar{\omega}_\nu; t'_\nu, \tau_\nu) E_{\nu' L}(t'_\nu) E_{\nu R}^\dagger(t'_\nu + \tau_\nu) \end{aligned} \quad (10)$$

$$\begin{aligned} & B^{(s,s',i,i')}(t'_s, \tau_s; t'_i, \tau_i) \\ &= T_L^{(s',i')}(t'_s, t'_i) T_R^{(s,i)\dagger}(t'_s + \tau_s, t'_i + \tau_i) \end{aligned} \quad (11)$$

is defined using the following superoperators corresponding to emission events

$$\begin{aligned} T_R^{(s',i'),\dagger}(t'_s, t'_i) &= i^2 \int_{-\infty}^{t'_2+\tau_2} dt_4 \int_{-\infty}^{t'_1+\tau_1} dt_3 \\ &\quad E_{sR}(t_3) E_{iR}(t_4) V_R^\dagger(t_4) V_R^\dagger(t_3) \\ T_L^{(s',i')}(t'_s, t'_i) &= i^2 \int_{-\infty}^{t'_2} dt_2 \int_{-\infty}^{t'_1} dt_1 \\ &\quad E_{sL}^\dagger(t_1) E_{iL}^\dagger(t_2) V_L(t_1) V_L(t_2) \end{aligned} \quad (12)$$

The averaging has been carried out over the two-exciton density operator following transport, i.e., $\rho_{f'f'}(t) = \mathcal{G}_{f'f',ff}(t - t')\rho_{ff}(t')$. Under a set of physically motivated approximations, the averaging can be carried out over each of these three terms independently. We also define the entangled photon driven excitation superoperator for future convenience, given by

$$\begin{aligned} O(t) &= T_R^\dagger(\tau_2, \tau_3) T_L(\tau_1, \tau_4) = i^2 \int_{-\infty}^{\tau'_2} d\tau_4 \int_{-\infty}^{\tau'_1} d\tau_3 \\ &\quad \int_{-\infty}^{\tau_3} d\tau_2 \int_{-\infty}^{\tau_4} d\tau_1 E_L^\dagger(\tau_4) E_L^\dagger(\tau_1) E_R(t_3) E_R(\tau_2) \\ &\quad V_R^\dagger(\tau_3) V_R^\dagger(\tau_2) V_L(\tau_4) V_L(\tau_1) \end{aligned} \quad (13)$$

In the above, we assume that the excitation and emis-

sion events are not temporally overlapping, which results in the signal in Eq. 9 being factorized in terms of three principal contributions: first, preparation, involving exciton-photon (driving fields) interactions that lead to the preparation of the two-exciton density operator; second, evolution, describing two-exciton transport over a parametric time interval; and third, detection, describing exciton-photon (detection fields) interactions that yield the time-frequency filtered two-photon coincidence. In subsequent sections, we systematically describe all three contributions.

A. Entangled photon-pair excitation

The quantity of interest at the preparation stage, the two-exciton population distribution, can be defined using a projection operator acting on the diagonal matrix elements of the phonon-averaged exciton density operator, expressed as: $\rho_{ff}(t) = \text{Tr}[O(t)|f\rangle\langle f|]_{\rho_0}$. Here, a factorizable initial condition between the driving, the detection field modes, and the exciton density operator is assumed. We perturbatively expand the combined photon-exciton-phonon density operator to the fourth order in $H_{\text{int}}(t)$, and partially trace over the phonon modes to obtain the desired expression for the observable (derivation detailed in Appendix B) as follows:

$$\begin{aligned} \rho_{ff}(t) &\propto 2\text{Re} \left\{ \int \frac{d\omega_4}{2\pi} \int \frac{d\omega_3}{2\pi} \int \frac{d\omega_2}{2\pi} \int \frac{d\omega_1}{2\pi} e^{+i\omega_3\tau_3+i\omega_4\tau_4-i\omega_2\tau_2-i\omega_1\tau_1} \langle E^\dagger(\omega_4) E^\dagger(\omega_3) E(\omega_2) E(\omega_1) \rangle \right. \\ &\quad \left\{ d_{fe'} d_{e'g} d_{fe}^* d_{eg}^* \times I(-\omega_4 - \omega_3 + \omega_2 + \omega_1; -z_{ff}) I(-\omega_3 + \omega_2 + \omega_1; -z_{fe'}) I(+\omega_2 + \omega_1; -z_{fg}) I(\omega_1; -z_{eg}) \right. \\ &\quad + d_{fe'} d_{fe}^* d_{e'g} d_{eg}^* \times I(-\omega_4 + \omega_2 - \omega_3 + \omega_1; -z_{ff}) I(\omega_2 - \omega_3 + \omega_1; -z_{fe''}) \\ &\quad \left(\delta_{ee'} \sum_p \chi_{e''p}^R D_{pp}^{-1} I(-\omega_3 + \omega_1; -z_p) \chi_{pe'}^L + (1 - \delta_{ee'}) \delta_{ee''} I(-\omega_3 + \omega_1; -z_{ee'}) \right) I(\omega_1; -z_{eg}) \\ &\quad + d_{fe'} d_{fe}^* d_{e'g} d_{eg}^* \times I(+\omega_2 - \omega_4 - \omega_3 + \omega_1; -z_{ff}) I(-\omega_4 - \omega_3 + \omega_1; -z_{fe''}) \\ &\quad \left. \left(\delta_{ee'} \sum_p \chi_{e''p}^R D_{pp}^{-1} I(-\omega_3 + \omega_1; -z_p) \chi_{pe'}^L + (1 - \delta_{ee'}) \delta_{ee''} I(-\omega_3 + \omega_1; -z_{ee'}) \right) I(\omega_1; -z_{eg}) \right\} \end{aligned} \quad (14)$$

It is a sum of five distinct terms that represent interfering exciton pathways (see Liouville space Feynman diagrams presented in Fig. 2 for more insights). It includes contributions from both one- and two-exciton coherence and population terms of the exciton density operator. The first term represents the two-exciton coherence-mediated pathway, which is susceptible to inter-manifold dephasing. The second and fourth terms describe pathways susceptible to one-exciton population transport. The third and fifth terms describe pathways susceptible to intra-manifold dephasing. The convolutional form is particu-

larly advantageous for introducing the field correlation functions, given in Eq. 6-Eq. 8. The field correlation functions can be manipulated to selectively suppress and amplify specific exciton resonances. Next, we illustrate these capabilities via numerical simulations for both degenerate and nondegenerate entangled photon pairs.

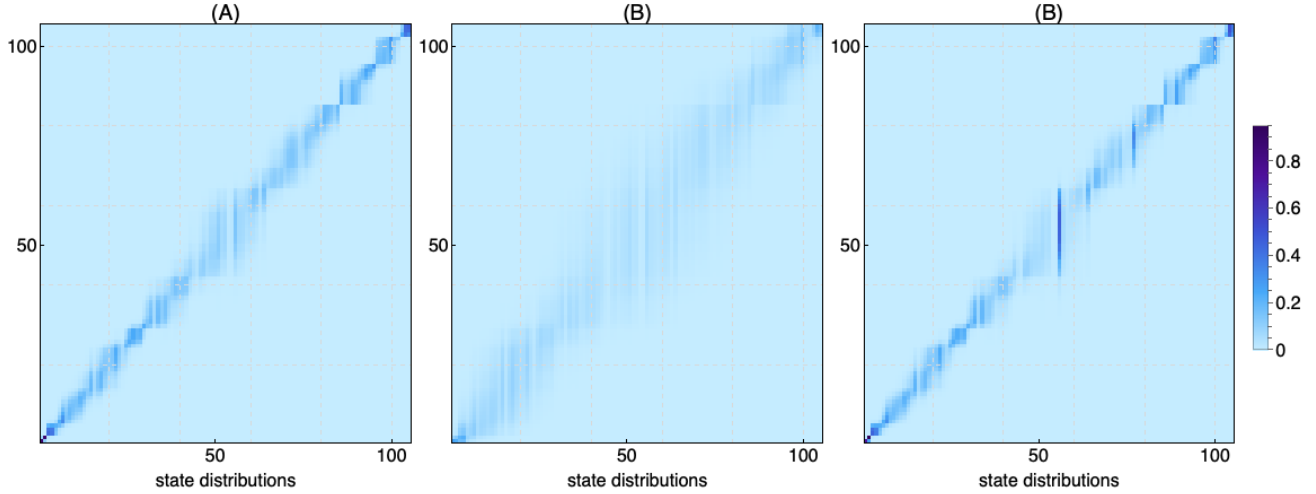


FIG. 3: The two-exciton population distribution map, constructed by sequentially targeting each of the 105 states in that manifold, using degenerate entangled photon pairs i.e., $\omega_i = \omega_p/2 = E_{\text{target}}^{(2)}/2$. The left panel serves as a reference simulation while the temporal width of the SPDC pump (entanglement time) is varied in the middle panel (right panel). Dispersal of the plot, in the horizontal cut, away from diagonal signifies a reduction in the narrowband excitation. For discussion, see section III A

1. Simulation: excitation of the full suite of two-exciton states using degenerate entangled photon pairs

2. Simulations: differential preparation of two-exciton populations via preselected mediating states and parametric dependence on photonic properties

In this section, we monitor the final population distribution following the excitation via spectrally degenerate entangled photon pairs, i.e., $\omega_1 = \omega_2 = \omega_p/2 = E_{\text{target}}^{(2)}/2$. We had carried out a parametric scan, taking each of the $N_f = 105$ two-exciton states as a target, and present the final normalized population distribution in Fig. 3. The simulation presented in the left column uses an entanglement time of $T_{\text{ent}} = 10$ fs and an SPDC pump width of $\tau_0 = 150$ fs, and acts as a reference case. Variations in the temporal width of the SPDC pump ($\tau_0 = 50$ fs) and the entanglement time parameter ($T_{\text{ent}} = 60$ fs) are presented in the middle and the right column, respectively. We note that target states near the middle of the energy ladder exhibited broader distributions around the target in all three cases. In other words, we find a lower degree of selectivity for target states in the middle rung of the two-exciton manifold and higher selectivity for those belonging to the lower rung. Altering the width of SPDC pump pulse in the middle column resulted in diminished selectivity, likely due to the activation of multiple pathways. Altering the entanglement time in the right column preserved the selectivity for the majority of states. Across all plots, we notice a trend: some two-exciton states remain preferentially populated across all parameter regimes. This feature have likely emerged from an intricate interplay of exciton transport parameters leading to the absence of specific relaxation channels.

Now, we focus on two specific two-exciton states, f_{07} and f_{83} , among the full suite of target states previously monitored, and examine the possibility of their excitation via a chosen pair one-exciton states, selected by setting $\omega_1 = E_{07}$ and $\omega_2 = E_{09}$. The mediating states are delocalized over sites and prone to ultrafast transport. The results are displayed in the left column of Fig. 4, and Fig. 5, respectively. The entanglement time and width of SPDC pump are set at $T_{\text{ent}} = 10$ fs and $\tau_0 = 150$ fs, for the upper panel (similar to the reference case in Fig. 3). The width is varied to $\tau_0 = 50$ fs in the middle panel, and the entanglement time is varied to $T_{\text{ent}} = 40$ fs in the bottom panel. The results demonstrate that the desired narrowband excitation is indeed possible, albeit with low final occupancy. The increase in the temporal width results in a significant loss of selectivity as the number of mediating pathways with comparable spectral weights grows. The variation of the entanglement time didn't result in any major changes, except for the tailoring of the relative populations. The latter, however, will have consequences as the population redistributes over time, as will be shown in the next section.

B. Transport in the two-exciton manifold

The created population distributions undergo time evolution governed by the parameters of the two-exciton transport matrix. Here, the following questions are worth investigating: What is the nature of the population evo-

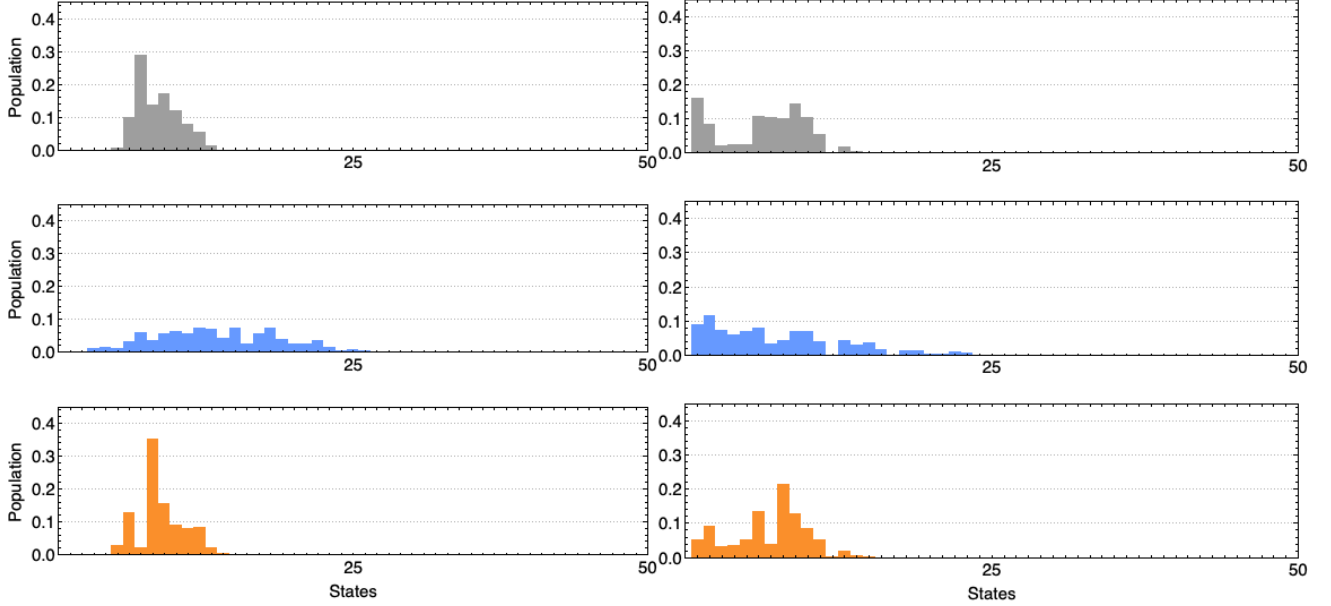


FIG. 4: The population distribution for the target state f_{07} which is dominantly excited via the intermediate states e_{07} and e_{09} is displayed for variations in the entangled photon parameters (rows) and for two distinct transport times (columns): $t = 0$ fs (immediately after the pulse) and $t = 50$ fs. In the upper panel, the entanglement time is $\tilde{T}_{\text{ent}} = 10$ fs and the SPDC pump width is $\tau_0 = 150$ fs. In the middle panel (lower panel), the width is reduced (entanglement time is increased) to $\tau_0 = 50$ fs ($\tilde{T}_{\text{ent}} = 30$ fs). For detailed discussion, refer to Section III A.

lution for a given state distribution? How do two initially created two-exciton population distributions undergo redistribution? And how does the nature of redistribution kinetics vary with driving field parameters?

The kinetic equation that governs the dissipative time evolution of exciton populations, i.e., exciton transport is given by

$$\frac{d}{dt}\rho_{ff}(t) = - \sum_{f'} K_{ff,f'f'}\rho_{f'f'}(t) \quad (15)$$

where the transport rate matrices, $K_{ff,f'f'}$ follow the detailed balance condition $K_{f'f',ff}/K_{ff,f'f'} = \exp(-\omega_{f'f}/(k_B T))$, and $\sum_f K_{ff,f'f'} = 0$. The initial two-exciton population distribution is obtained via the Eq. 14 which is propagated using the expression: $\rho_{ff}(t_2) = G_{ff,f'f'}^{(N)}(t_2-t_1)\rho_{f'f'}(t_1)$, where the $G_{f'f',ff}^{(N)}(\tau)$ is given by first term in Eq. 3. The following four sets of simulations will help us address the questions posed above.

1. Simulations: differential evolution of two-exciton populations and parametric dependence on photonic properties

We track the differential population evolution following the excitation targeted at f_{07} (right column in Fig. 4) and f_{83} (right column in Fig. 5), taken at a delay of $t = 50$ fs, and $t = 250$ fs, respectively. Each of the three panels, up-

per, middle and bottom, represents simulation using different photonic parameters. The parameters were listed in the preceding section III A 2 where we discussed the reference simulation. We observe that the evolved distributions at short times retained the memory of prepared distribution in Fig. 4, but gets washed out in Fig. 5. The effect of the variation of photonic parameters is also less visible in the latter. The rapid redistribution and localization towards a few selected states in the latter is a key feature that requires future investigation. It can also be concluded that such a prepared distribution would loose the principal advantages of the entangled photon pair excitations.

2. Simulations: differential redistribution of two-exciton populations

In Fig. 6, we track the population redistribution by displaying the population snapshots at $t = 50, 100, 250, 1000$ fs following the excitation targeted at f_{07} (in the left column) and f_{83} (in the right column). The results demonstrate two distinct features: the population migrates to the lower energy sector of the manifold rather monotonically for f_{07} and by a slower intra-manifold cascading mechanism for f_{83} . The slower transport can be attributed to lack of overlap between the latter with the state in the middle rung of two-exciton manifold.

The population redistribution can be spectroscopi-

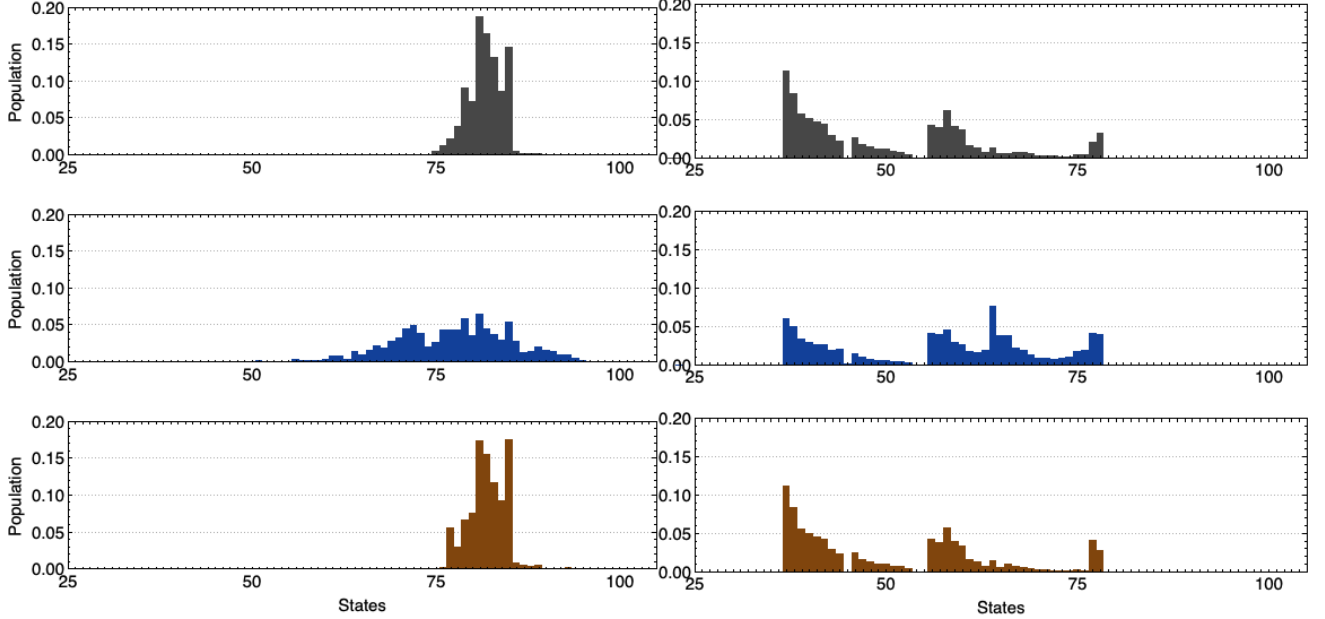


FIG. 5: The population distribution for the target state f_{83} which is dominantly excited via the intermediate states e_{07} and e_{09} is displayed for variations in the entangled photon parameters (rows) and for two distinct transport times (columns): $t = 0$ fs (immediately after the pulse) and $t = 250$ fs. In the upper panel, the entanglement time is $\tilde{T}_{\text{ent}} = 10$ fs and the SPDC pump width is $\tau_0 = 150$ fs. In the middle panel (lower panel), the width is reduced (entanglement time is increased) to $\tau_0 = 50$ fs ($\tilde{T}_{\text{ent}} = 30$ fs). For detailed discussion, refer to Section III A.

cally monitored by combining spectral-temporal filtering schemes in the detection of the two-photon emission. [44, 51, 53]. Such a scheme will track cascaded inter-manifold transitions fluorescence that competes with the intra-manifold transport. The next section is devoted to the theory and simulations demonstrates these schemes.

C. Multipoint photon correlation spectroscopy

The quantity of interest in photon correlation spectroscopy is the time-frequency filtered two-photon coincidence counting signal. In this section, we describe how this quantity can monitor the time-evolved population distributions that serve as the initial configuration for the photon emission pathways. The signal can be expressed as:

$$\begin{aligned}
 S(\{\bar{t}_j, \bar{\omega}_j\}) &= \int dt'_1 \int d\tau_1 D^{(1)}(t_1, \omega_1; t'_1, \tau_1) \\
 &\times \int dt'_2 \int d\tau_2 D^{(2)}(t_2, \omega_2; t'_2, \tau_2) \langle N_r(t'_1, \tau_1) N_s(t'_2, \tau_2) \rangle \\
 &= \int dt'_1 \int d\tau_1 \int dt'_2 \int d\tau_2 D^{(1)}(t'_1, \tau_1) D^{(2)}(t'_2, \tau_2) \\
 &\sum_{s,s'} \sum_{i,i'} \langle E_{s'}^\dagger(t'_2 + \tau_2) E_i^\dagger(t'_1 + \tau_1) E_i(t'_1) E_s(t'_2) \rangle \quad (16)
 \end{aligned}$$

where $N(t', \tau) = \sum_{s,s'} \hat{E}_{sR}^\dagger(t' + \tau) \hat{E}_{s'L}(t')$ is a bare photon number operator and $E_s(t) = \sqrt{2\pi\hbar\omega_s/\Omega} \hat{a}_s e^{-i\omega_s t}$,

and Ω is the mode quantization volume corresponding to the detector modes. We also defined two detector spectrogram functions: $D^{(j)}(\bar{t}_j, \bar{\omega}_j; t'_j, \tau_j)$ that are governed by the parameters \bar{t}_j and $\bar{\omega}_j$, describing the detector centering times for the temporal, and spectral filter, respectively. It can be expressed in terms of the filtering functions as,

$$\begin{aligned}
 D(\bar{t}, \bar{\omega}, t', \tau) \\
 = \int \frac{d\omega''}{2\pi} e^{-i\omega''\tau} |F_{\bar{\omega}}(\omega'', \omega)|^2 F_t^*(t' + \tau, t) F_{\bar{t}}(t', t). \quad (17)
 \end{aligned}$$

Modulation of these functions individually allows for the examination of the photon emission pathways and the systematic recovery of the photon correlation functions. For this work, we choose the Lorentzian filtering functions (see Appendix D), which leads to the spectrogram being expressed as:

$$\begin{aligned}
 D(\bar{t}, \bar{\omega}, t', \tau) &= \frac{1}{2\sigma_\omega} \theta(t' - t) \theta(t' + \tau - t) \\
 &[\theta(\tau) e^{-\sigma_\omega \tau} + \theta(-\tau) e^{\sigma_\omega \tau}] e^{-(i\omega + \sigma_t)\tau - 2\sigma_t(t' - t)} \quad (18)
 \end{aligned}$$

We lay out the filtering strategy: the spectral filters allow state-resolution for the dynamics occurring within similar transport windows; the temporal filters help separate the transport processes that involve transitions with similar energy gaps; combined together, they allow for the tracking of individual state transitions. The filtering properties are controlled by the width of the temporal

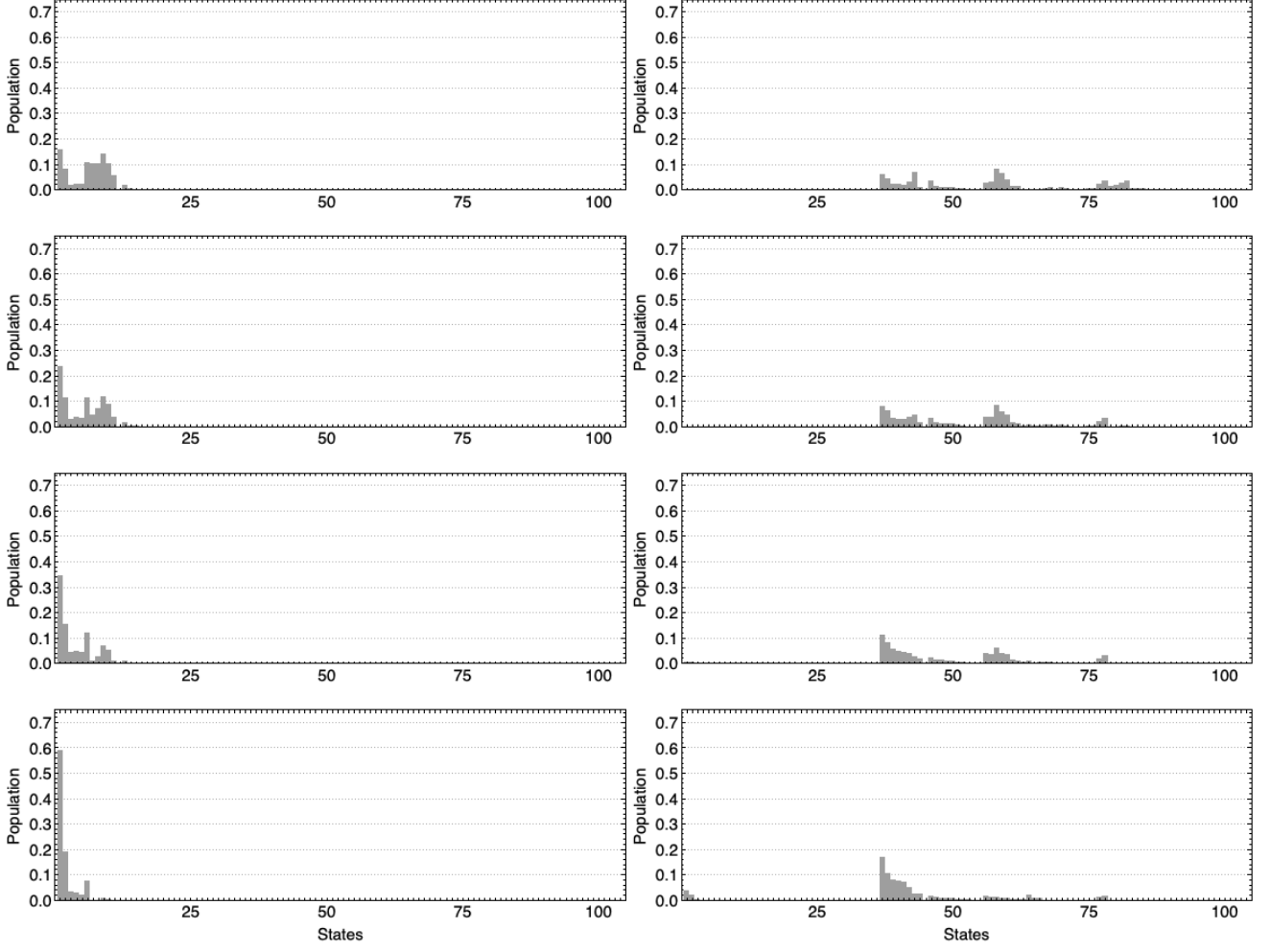


FIG. 6: Population redistribution at four different time points following the excitation of the target states f_{07} (right column) and f_{83} (left column). The results demonstrate key features of the dynamics, including rapid funneling of the population along energy gradients and cascaded population migration for the two targets, respectively. For detailed discussion, refer to Section III B

(spectral) filters, $\sigma_{\bar{\omega}_j}(\sigma_{\bar{t}_j})$, centering times of the temporal (spectral) gate, t_j ($\bar{\omega}_j$). The final signal can be

expressed as the sum of four pathways (which is reduced to two following symmetry arguments):

$$\begin{aligned}
 S(\{\bar{t}_j, \bar{\omega}_j\}) &= \sum_{p=1}^4 S^{(p)}(\{\bar{t}_j, \bar{\omega}_j\}) = 2\text{Re} \sum_{p=1}^2 S^{(p)}(\{t_j, \omega_j\}) \\
 &= \sum_{g,e,e',f,f'} |\mathcal{D}(\omega_1)\mathcal{D}(\omega_2)|^2 |d_{eg}|^2 |d_{ef}|^2 \times \int dt'_1 \int d\tau_1 D_{>}^{(1)}(\bar{t}_1, \bar{\omega}_1; t'_1, \tau_1) \times \int dt'_2 \int d\tau_2 D_{>}^{(2)}(\bar{t}_2, \bar{\omega}_2; t'_2, \tau_2) \\
 &\quad \langle \langle I | \mathcal{G}_{ge',ge'}(\tau_1) \mathcal{G}_{e'e',ee}(t'_1 - t'_2 - \tau_2) \mathcal{G}_{ef',ef'}(\tau_2) \mathcal{G}_{f'f',ff}(t'_2) | \rho_{ff} \rangle \rangle \\
 &\quad + \sum_{g,e,e',f,f'} |\mathcal{D}(\omega_1)\mathcal{D}(\omega_2)|^2 |d_{eg}|^2 |d_{ef}|^2 \times \int dt'_1 \int d\tau_1 D_{>}^{(1)}(\bar{t}_1, \bar{\omega}_1; t'_1, \tau_1) \times \int dt'_2 \int d\tau_2 D_{<}^{(2)}(\bar{t}_2, \bar{\omega}_2; t'_2, \tau_2) \\
 &\quad \langle \langle I | \mathcal{G}_{ge',ge'}(\tau_1) \mathcal{G}_{e'e',ee}(t'_1 - t'_2) \mathcal{G}_{f'e',f'e}(-\tau_2) \mathcal{G}_{f'f',ff}(t'_2 + \tau_2) | \rho_{ff} \rangle \rangle
 \end{aligned} \tag{19}$$

The terms $D_{>}$ and $D_{<}$ indicate the sign of the delay τ

variables, and $\mathcal{D}(\omega_1)\mathcal{D}(\omega_2)$ is the density of states for the

detector, taken at an idealized, narrowband limit around each frequency ω_j . In our simulation, the influence of this delay was accounted for by evaluating the action of the transport Green's functions on the initial states within the respective manifolds.

The rationale for deploying such a scheme can be developed in the following manner. During population transport, the ensuing redistribution erases the signatures of the initially created two-exciton wavepacket. The timescales of this phenomena depend on the properties of the transport Green's functions. The redistribution give rise to new inter-manifold dipole-allowed transitions and render some transitions diminished in spectral intensity. The subsequent photon emission events can be monitored by appropriately selecting the spectral and temporal filtering properties of the first set of detectors. Following the photon emission, the dynamics continue in the one-exciton manifold where transport population scrambling takes place for a time interval, followed by another photon emission event to the ground state. Three representative pathways in Fig.1 shows complexities that may be present.

The joint spectral-temporal filtering strategy can be a powerful tool that enhances the resolution of the bare photon coincidence counting signal. Two sets of spectral-temporal filters, defined by the spectrogram can accomplish two distinct tasks: first, the photon emissions events can be temporally windowed to focus on transport timescales and spectrally windowed to focus on the relevant exciton states; second, the photon emissions events can be spectrally windowed such that pairs of inter-manifold transitions originating from the similar two-exciton transport events can be monitored. Monitoring these events allows us to construct a kinetic description of dissipative exciton dynamics events triggered by the entangled photon excitation. It also help infer how long the remnants of the initially created wavepacket persist. The diagrams presented in Figure 2 clarify the physical processes in a more transparent manner.

1. Simulation: two-photon coincidence counting signal with variation in filtering parameter and different waiting times

In Fig. 7, we present six two-dimensional plots illustrating the signal where the filtering widths and centering parameters (the latter relates to the transport times) are varied. The centering times of the spectral filters are taken as the scanning parameters. In these plots, a series of features can be noticed: the peaks along the $\bar{\omega}_1$ axis correspond to transitions from the two to and one-exciton manifold ($\sim \omega_{fe}$), while the peaks along the $\bar{\omega}_2$ axis correspond to transitions from the one-exciton manifold to the ground state ($\sim \omega_{eg}$). The one-exciton manifold has a spectral width of $\approx 950 \text{ cm}^{-1}$. The density of energy gaps is significantly higher in the upper set of transitions. Even though, for the chosen example, the initial state distribution, following excitation of f_{07} , ef-

fectively spans only the first ten levels of the two-exciton manifold (an energy range of $\approx 350 \text{ cm}^{-1}$), the number of possible ω_{fe} transitions remains high.

The upper-left panel (the reference simulation for this set) employs the following filtering parameters: spectral widths $\sigma_{\bar{\omega}_1} = \sigma_{\bar{\omega}_2} = 10 \text{ cm}^{-1}$, temporal widths $\sigma_{\bar{t}_1} = \sigma_{\bar{t}_2} = 4.8681 \text{ cm}^{-1}$, and two-exciton (one-exciton) waiting times $t_{w,1} = 0 \text{ fs}$ ($t_{w,2} = 100 \text{ fs}$). Variables $t_{w,j}$ are associated with the t_2, t_1 integrals when the detector spectrograms are inserted into the relevant expression. We observe eight resonance zones spread along the $\bar{\omega}_1(/10^3 \text{ cm}^{-1})$ axis, each containing several resonances that can be resolved along the $\bar{\omega}_2(/10^3 \text{ cm}^{-1})$ axis. For easier interpretation, we may classify these resonances along $\bar{\omega}_1$ as four distinct clusters, containing the following number of resonance zones: two ($\sim 14.0 - 14.2$), three ($\sim 14.3 - 14.7$), two ($\sim 14.9 - 15.1$), and one ($\sim 15.3 - 15.5$). Each of these clusters may have multiple origins in the upper manifold. The four observed $\bar{\omega}_1$ resonance clusters correspond approximately to the transitions $\omega_{f_1e_{13}}$ and $\omega_{f_2e_{10}} - \omega_{f_2e_{13}}$; $\omega_{f_1e_8}, \omega_{f_2e_6}, \omega_{f_2e_5}$; $\omega_{f_4e_3}$ and either $\omega_{f_3e_1}$ or $\omega_{f_4e_1}$; and $\omega_{f_7e_1} - \omega_{f_8e_1}$, respectively. Taking each cluster, the $\bar{\omega}_2(/10^3 \text{ cm}^{-1})$ resonances are located at $\sim 15.5, 15.8$ and $\sim 15.4, 15.7$ (corresponding to $\omega_{e_{8g}}, \omega_{e_{12g}}$ and $\omega_{e_{8g}}, \omega_{e_{12g}}$); $\sim 15.3, 15.6$, $\sim 15.3, 15.4$, and $\sim 15.3, 15.4$ ($\omega_{e_{7g}}, \omega_{e_{8g}}$; $\omega_{e_{7g}}, \omega_{e_{8g}}$; and $\omega_{e_{7g}}, \omega_{e_{8g}}$); $\sim 15.1, 15.3$ ($\omega_{e_{1g}}, \omega_{e_{3g}}$); and ~ 15.0 ($\omega_{e_{1g}}$), respectively. This plot will serve as a reference simulation.

The upper-right panel presents the results of varying the spectral filter width by setting $\sigma_{\bar{\omega}_1} = \sigma_{\bar{\omega}_2} = 20 \text{ cm}^{-1}$, while keeping all other parameters fixed to those of the reference simulation. We observe that several resonance zones in the second cluster are absent along the $\bar{\omega}_1$ axis, with the most noticeable absences occurring in the middle and lower energy sectors. Additionally, among the present zones, a few resonances along the $\bar{\omega}_2$ axis are absent, and the fourth cluster has been diminished in intensity. This observation may be rationalized by noting the increased destructive interferences permitted by the broadband spectral filter.

The middle-left panel investigates the effect of longer waiting times, specifically using $t_{w,2} = 1000 \text{ fs}$ for the one-exciton transport, while keeping all other parameters unchanged from the reference simulation. The population distribution in the one-exciton manifold is dependent on the cascaded emission from the two-exciton manifold. We note that the clusters have further coalesced along the $\bar{\omega}_1$ axis and are clearly separated into two dominant regions. The latter is indicative of the dipole transition rule dominating the spectral weight at these longer times. Furthermore, the fourth cluster has vanished, and the resolution along the $\bar{\omega}_2$ axis is lost. The middle-right panel explores the variation of resolution compared to the middle-left one by varying both the spectral filter width and the one-exciton waiting time ($t_{w,2}$). The parameters are set jointly equal to those used in the two previous simulations ($\sigma_{\bar{\omega}_1} = \sigma_{\bar{\omega}_2} = 20 \text{ cm}^{-1}$ and $t_{w,2} = 1000 \text{ fs}$), while keeping all other parameters fixed. We observe

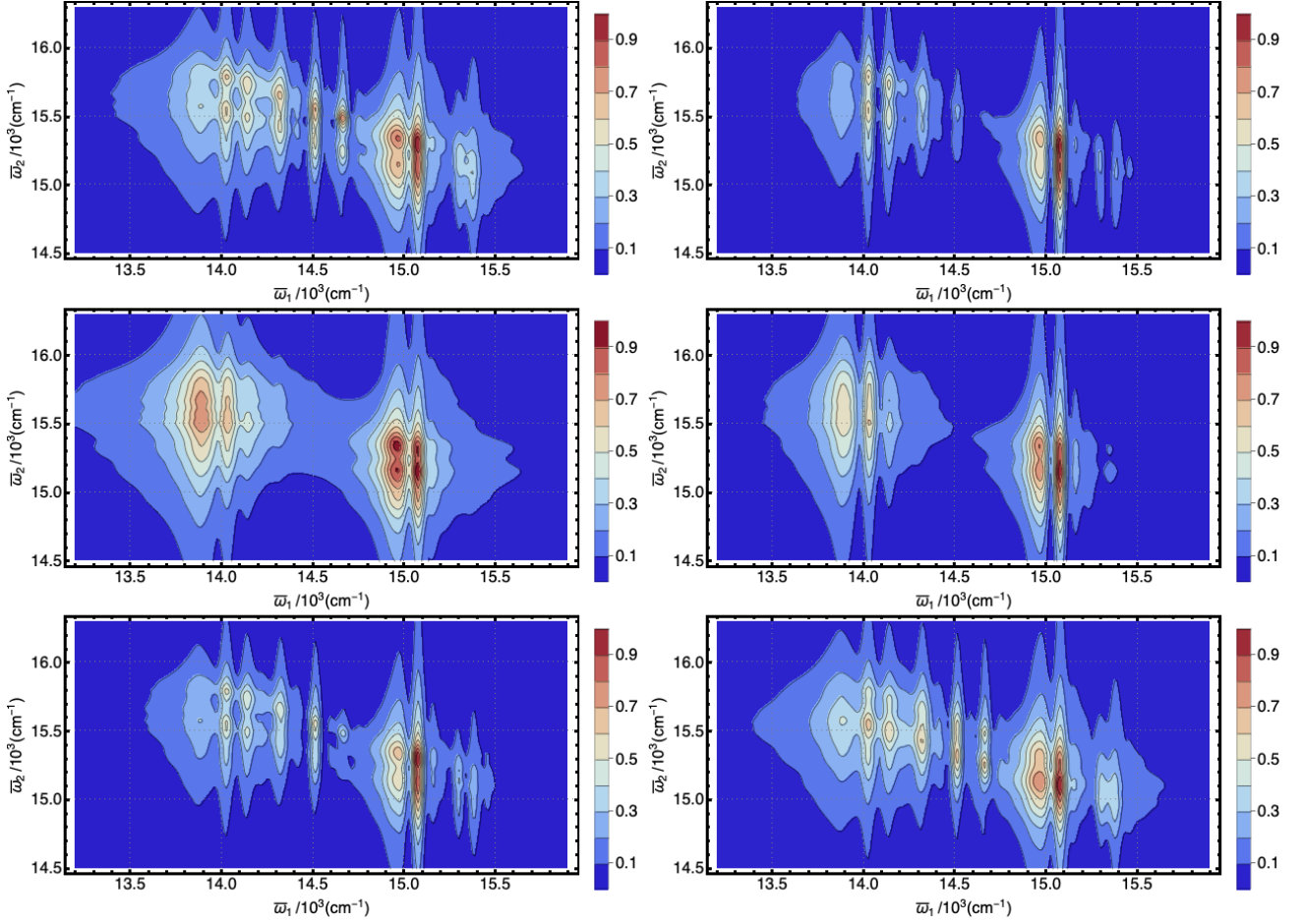


FIG. 7: The time-frequency filtered two-photon coincidence counting signal is displayed, showing variations in the widths of both filtering functions and the centering time of the temporal filtering function. To control the signal resolution, the following systematic variations relative to the reference simulation (upper-left) are presented: the width of the spectral filter (upper-right); the centering time of the temporal filtering function (middle-left); both the spectral filter width and the temporal filter centering time (middle-right); the width of the temporal filter (bottom-left); and the centering time of the temporal filtering function (bottom-right). The targeted excitation of f_{07} by the entangled photon pairs serves as the initial configuration, which is followed by a subsequent series of events: two-exciton manifold transport, inter-manifold transitions, one-exciton manifold transport, and subsequent inter-manifold transitions. For a diagrammatic illustration of the processes involved, see Fig. 2, and for detailed discussion, refer to Section III C 1

that widening the spectral gate may not have permitted a larger number of resonance structures along the $\bar{\omega}_2$ axis. This implies that a broader set of transitions remain unaccounted for (either not presented or not dipole allowed). Importantly, these transitions, despite differing widely in energy, participate in similar dynamics due to the longer transport window afforded by the extended waiting time.

The lower panels are dedicated to exploring two distinct cases: the bottom-left panel examines the role of the width of the temporal filter (by setting $\sigma_{\bar{\omega}_2} = 0.5409 \text{ cm}^{-1}$), and the bottom-right panel examines the role of the two-exciton transport waiting time (by setting $t_{w,1} = 50 \text{ fs}$), while keeping other parameters the

same as the reference. For the bottom-left panel, we note that the second cluster has a diminished presence, with several resonances along the $\bar{\omega}_2$ axis being absent, an effect attributed to the shorter temporal filter effectively skipping some transitions occurring at longer respective timescales. For the bottom-right panel, in contrast with the reference simulation, we observe that the double resonance structures along the $\bar{\omega}_2$ axis have coalesced into single structures, while there is no significant change along the $\bar{\omega}_1$ axis. This can be attributed to the fact that at longer two-exciton transport duration, state-specific transport rates exhibited minor differences. The redistributed the spectral weights, in turn, has resulted in a fewer ω_{fe} transitions becoming dominant.

The initial states in all cases can be tracked from Figure 6. However, the state indices require a conversion to the energy domain (energy gaps) for constructing a robust phenomenological description.

IV. CONCLUSIONS

In this article, we had demonstrated that a combined protocol utilizing entangled photon-pair excitation and temporally-spectrally filtered photon counting provides a systematic route to probe dissipative multi-exciton kinetics. The protocol, illustrated via simulations for the exciton aggregate LHCII, is presented across three subsequent sections. It revealed, in section III A, that narrow-band distribution around a special class of two exciton states can indeed be excited with considerable degree of control. The final population distribution is benchmarked against the variation of the entangled photon parameters in section III A 2. Here we examined the pathway selectivity by targeting two different two exciton state that are excited via two pre-selected one-exciton states. The exciton-phonon interactions in multi-site molecular aggregates are characterized by exciton transport and dephasing dynamics spanning multiple time and energy scales. The entangled photon pairs demonstrated a superior ability maintain pathway selectivity. Following the excitation, and population evolution, illustrated in section III B 1-III B 2), we introduced the detection scheme to monitor the fate of the time-evolving population, and classify the emission pathways. It was shown, in section III C, that the joint spectral and temporal filtering of the emitted fluorescence allow a more nuanced monitoring of inter-manifold transitions competing with intra-manifold transport kinetics.

We note that the targeted states, in III A 2, are chosen due to their higher overlap with the local overtone states. These properties can be quantified by analyzing the transformation matrix elements, $T_{k,mm}^{(2)}$. While state-selective excitations in interacting molecular aggregates conventionally yield spatially delocalized wavepackets, an important corollary suggests that a specially crafted exciton wavepacket, that is, a tailored superposition of exciton eigenstates, may allow for the excitation of spatially localized wavepackets. Such localization could then enhance the propensity of exciton-exciton annihilation provided that significant non-adiabatic coupling elements between the higher-lying states allow the internal conversion to occur.

The expression in Eq. 14 remains valid for a wide range of correlated optical fields, albeit in the weak-field regime. In the expression, five terms appear, each of which contains a convolution of inter-manifold coherence and intra-manifold population Green's functions with four-point photon correlation functions. The latter can be interpreted as pathway weights, and multiobjective optimization schemes can be used to actively design them. Future work will address this issue.

Similarly, the expressions in Eq. 19 remain valid for any general initial state distributions. The variation of the filtering parameters offers us the ability to classify inter-manifold transitions in the presence and competing with intra-manifold transport kinetics. It allows better assignment timescales and generate a dynamical picture for one and two-exciton transport kinetics. We assumed that the excitation and emission events are temporally separated, omitting spontaneous Raman contributions.

From these simulations, a probing strategy may emerge: preferentially accessing the one-exciton resonances that are less susceptible to transport within a given temporal window may be the key to achieving controlled excitation. We note that the full protocol encountered transport events thrice during its course. Within the model and the chosen expressions, the entanglement time, controlled by the length of the birefringent crystal, determines the temporal window of the photon-exciton interactions. The bandwidth of the classical SPDC pump, on the other hand, determines the range of accessible resonances. The independent controllability of these variables affords some flexibility in selecting their values. In turn, it will allow control over a broad range of time and frequency parameter domain. Analogously, the choice of filtering parameters, decided independently, must take into account the excitation properties to be able to characterize a wide range of two-photon emission pathways. The utility of correlated photonic sources for multiphoton spectroscopies promises two main advantages in the appropriate parameter regime: the ability to actively modulate multiple material pathways to highlight unseen spectral signatures, and favorable scaling of the signal with the incoming field intensity. However, these benefits face a significant challenge due to the inherently weak signal-to-noise ratio. Technological advances in this direction would make the proposed protocol a suitable investigative tool for exploring potential non-classical effects in light-harvesting complex. Alternatively, the scheme remains applicable in the high-gain regime using squeezed photon sources.

ACKNOWLEDGMENTS

A.D. acknowledges the support from DESY (Hamburg, Germany), a member of the Helmholtz Association HGF. S.M. gratefully acknowledges the support of the National Science Foundation (NSF) grant Grant No. CHE-2246379.

Appendix A: The Hamiltonian

In the Hamiltonian, the Eq. 1, the vibrational terms are specified in the third line. The normal modes associated with collective intermolecular vibrations constitute the phonon modes. The latter, in the continuum limit, i.e., $J_{\text{ph}}(\omega) = \sum_j |g_j|^2 [\delta(\omega - \omega_j) - \delta(\omega + \omega_j)]$ are described

using an overdamped oscillator and 48 multimode Brownian oscillators. The corresponding spectral function is given by

$$J_{\text{ph}}(\omega) = 2\lambda_0 \frac{\omega\gamma_0}{\omega^2 + \gamma_0^2} + \frac{2\lambda_j\omega_j^2\omega\gamma_j}{(\omega_j^2 - \omega^2)^2 + \omega^2\gamma_j^2} \quad (\text{A1})$$

Here, λ_0 and γ_0 represent the damping strength and relaxation parameter for the overdamped mode, respectively. The Brownian oscillators are characterized by the Huang-Rhys parameter, mode frequency, and correlation time, denoted as λ_j , γ_j , ω_j , respectively. Relevant parameter values are detailed in the [27, 52].

The phonon interaction gives rise to exciton transport (first term) and dephasing (second term) Eq. 3. The exciton transport components can be expressed as

$$[\exp(-K^{(n)}t)]_{a_1a_1, a_3a_3} = \sum_p \chi_{a_1p}^R D_{pp}^{-1} e^{-\lambda_p t} \chi_{pa_3}^L \quad (\text{A2})$$

where λ_p is the p-th eigenvalue of the transport matrix, $\chi^L(\chi^R)$ are the left (right) eigenvectors $K\chi^R = \lambda_p \chi^R$ and $\chi^L K = \lambda_p \chi^L$ of the same with additional relation $D_{pp} = \chi^L \chi^R$. The inter-manifold coherence green's functions, contains excitonic resonances $i\omega_{a_1a_2}^{(n)} - \gamma_{a_1a_2}^{(n)}t = z_{a_1a_2}^{(n)}$, where the line-broadening function term is evaluated as

$$\gamma_{a_j}^{(n)}(t) = \sum_{a_{j'}} C_{\text{ph}}(\omega_{a_j a_{j'}}^{(n)}) \sum_m T_{ma_j}^{(n)} T_{ma_j}^{(n)} T_{ma_{j'}}^{(n)} T_{ma_{j'}}^{(n)} \quad (\text{A3})$$

and the phonon correlation function evaluated at resonant exciton transition frequencies is given by

$$C_{\text{phonon}}(\Omega) = \int_0^\infty dt \exp(i\Omega t) \times \int \frac{d\omega}{2\pi} J(\omega) \left[\coth(\beta\omega/2) \cos\omega t \mp i \sin\omega t \right] \quad (\text{A4})$$

Therefore characteristic broadening of the resonances is determined by the phonon spectral function, and exciton gaps.

Appendix B: Note on the observable: two-exciton population distribution

The observable is defined using the projection operator onto the desired two-exciton state, averaged over the time-dependent density operator. Assuming the perturbative regime of exciton-driving field interaction to hold, the density operator can be expanded to the fourth-order in incoming field-exciton interaction Hamiltonian to obtain

$$\begin{aligned} O_{ff}(t) &= (-i)^4 \text{Re} \int_{-\infty}^\infty d\tau_4 \int_{-\infty}^{\tau_4} d\tau_3 \int_{-\infty}^{\tau_3} d\tau_2 \int_{-\infty}^{\tau_2} d\tau_1 \left\langle P_+(t) H_{\text{int},R}(\tau_3) H_{\text{int},R}(\tau_2) H_{\text{int},L}(\tau_4) H_{\text{int},L}(\tau_1) \right\rangle \\ &= (-i)^4 \text{Re} \int_{-\infty}^\infty dt_4 \int_0^\infty dt_3 \int_0^\infty dt_2 \int_0^\infty dt_1 \langle P_+ \mathcal{G}(t_4) d_R \mathcal{G}(t_3) d_R \mathcal{G}(t_2) d_L^\dagger \mathcal{G}(t_1) d_L^\dagger \rangle \\ &\quad \langle E^\dagger(t-t_4) E^\dagger(t-t_4-t_3) E(t-t_4-t_3-t_2) E(t-t_4-t_3-t_2-t_1) \rangle \end{aligned} \quad (\text{B1})$$

In the expression using superoperator notation [51, 54], the variables τ_j denoted the exciton-photon interaction times in the first line. It is converted into time-delays $t_j = \tau_{ij} = \tau_i - \tau_j$ in the subsequent line. The field expression correlate the exciton evolution via the time

integrals. Expanding the exciton correlation function in the basis of one and two-exciton states, and carrying out the implicit averaging over the phonons lead to an computable expression of the signal which contains the exciton Green's functions (defined in Eq. 3). We further recast the expression in the frequency domain to obtain

$$\begin{aligned}
O_{ff}(t) = 2 \operatorname{Re} \Big\{ & \int \frac{d\omega_4}{2\pi} \int \frac{d\omega_3}{2\pi} \int \frac{d\omega_2}{2\pi} \int \frac{d\omega_1}{2\pi} e^{+i\omega_3\tau_3+i\omega_4\tau_4-i\omega_2\tau_2-i\omega_1\tau_1} \langle E^\dagger(\omega_4) E^\dagger(\omega_3) E(\omega_2) E(\omega_1) \rangle \\
& \left\{ d_{fe'} d_{e'g} d_{fe}^* d_{eg}^* \times \mathcal{G}_{ff}(-\omega_4 - \omega_3 + \omega_2 + \omega_1) \mathcal{G}_{fe'}(-\omega_3 + \omega_2 + \omega_1) \mathcal{G}_{fg}(\omega_2 + \omega_1) \mathcal{G}_{eg}(+\omega_1) \right. \\
& + d_{fe''} d_{fe'}^* d_{eg} d_{eg}^* \times \mathcal{G}_{ff}(-\omega_4 + \omega_2 - \omega_3 + \omega_1) \mathcal{G}_{fe''}(+\omega_2 - \omega_3 + \omega_1) \mathcal{G}_{e''e'',ee}(-\omega_3 + \omega_1) \mathcal{G}_{eg}(+\omega_1) \\
& + d_{fe'} d_{fe}^* d_{e'g} d_{eg}^* \times \mathcal{G}_{ff}(-\omega_4 + \omega_2 - \omega_3 + \omega_1) \mathcal{G}_{fe'}(+\omega_2 - \omega_3 + \omega_1) \mathcal{G}_{ee'}(-\omega_3 + \omega_1) \mathcal{G}_{eg}(+\omega_1) \\
& + d_{fe''}^* d_{fe'} d_{eg} d_{eg}^* \times \mathcal{G}_{ff}(+\omega_2 - \omega_4 - \omega_3 + \omega_1) \mathcal{G}_{e''f}(-\omega_4 - \omega_3 + \omega_1) \mathcal{G}_{e''e'',ee}(-\omega_3 + \omega_1) \mathcal{G}_{eg}(+\omega_1) \\
& \left. + d_{fe}^* d_{fe'} d_{e'g} d_{eg}^* \times \mathcal{G}_{ff}(+\omega_2 - \omega_4 - \omega_3 + \omega_1) \mathcal{G}_{ef}(-\omega_4 - \omega_3 + \omega_1) \mathcal{G}_{e'e}(-\omega_3 + \omega_1) \mathcal{G}_{eg}(+\omega_1) \right\} \quad (B2)
\end{aligned}$$

In expression above is significantly more detailed. Here five types of phonon-averaged exciton Green's functions, representing one, and two-exciton inter-manifold coherence, one and two-exciton transport and one-exciton intra-manifold coherence appear. They also bear accumulated frequencies of the driving field in their arguments. The first term represents the two-exciton

coherence-mediated pathways, the second and fourth terms represents one-exciton transport-mediated pathways and the third and fifth terms represents the one-exciton coherence-mediated pathways. A more explicit form of the expression can be obtained if we plug in the expressions of the exciton Green's functions. It gives

$$\begin{aligned}
O_{ff}(t) \propto 2 \operatorname{Re} \Big\{ & \int \frac{d\omega_4}{2\pi} \int \frac{d\omega_3}{2\pi} \int \frac{d\omega_2}{2\pi} \int \frac{d\omega_1}{2\pi} e^{+i\omega_3\tau_3+i\omega_4\tau_4-i\omega_2\tau_2-i\omega_1\tau_1} \langle E^\dagger(\omega_4) E^\dagger(\omega_3) E(\omega_2) E(\omega_1) \rangle \\
& \left\{ \frac{d_{fe'}}{-\omega_4 - \omega_3 + \omega_2 + \omega_1 - z_{ff}} \frac{d_{e'g}}{-\omega_3 + \omega_2 + \omega_1 - z_{fe'}} \frac{d_{fe}^*}{+\omega_2 + \omega_1 - z_{fg}} \frac{d_{eg}^*}{\omega_1 - z_{eg}} \right. \\
& + \frac{d_{fe''}}{-\omega_4 + \omega_2 - \omega_3 + \omega_1 - z_{ff}} \frac{d_{fe''}^*}{\omega_2 - \omega_3 + \omega_1 - z_{fe''}} \\
& d_{e'g} \left(\delta_{ee'} \sum_p \chi_{e''p}^R D_{pp}^{-1} \frac{1}{-\omega_3 + \omega_1 - z_p} \chi_{pe'}^L + (1 - \delta_{ee'}) \delta_{ee''} \frac{1}{-\omega_3 + \omega_1 - z_{ee'}} \right) \frac{d_{eg}^*}{\omega_1 - z_{eg}} \\
& + \frac{d_{fe''}^*}{+\omega_2 - \omega_4 - \omega_3 + \omega_1 - z_{ff}} \frac{d_{fe''}}{-\omega_4 - \omega_3 + \omega_1 - z_{fe''}} \\
& \left. d_{e'g} \left(\delta_{ee'} \sum_p \chi_{e''p}^R D_{pp}^{-1} \frac{1}{-\omega_3 + \omega_1 - z_p} \chi_{pe'}^L + (1 - \delta_{ee'}) \delta_{ee''} \frac{1}{-\omega_3 + \omega_1 - z_{ee'}} \right) \frac{d_{eg}^*}{\omega_1 - z_{eg}} \right\} \quad (B3)
\end{aligned}$$

A compact version of this expression, using the abbreviation $I(\omega_j; z_{ab}) = (\omega_j + z_{ab})^{-1}$ is presented in Eqn. 14.

Proceeding via tedious yet straightforward frequency integrations yields the expression below

$$\begin{aligned}
O_{ff}(t) \propto 2 \operatorname{Re} \Big[& \exp(z_{ff}t) \left(d_{fe'} d_{e'g} d_{fe}^* d_{eg}^* \times \langle E^\dagger(z_{fe'} - z_{ff}) E^\dagger(z_{fg} - z_{fe'}) E(-z_{eg} + z_{fg}) E(z_{eg}) \rangle \right. \\
& + d_{fe''} d_{fe'}^* d_{e'g} d_{eg}^* \times \langle E^\dagger(+z_{fe''} - z_{ff}) E(-z_p + z_{fe''}) \sum_p \chi_{e''p}^R D_{pp}^{-1} E^\dagger(z_{eg} - z_p) \chi_{pe}^L E(z_{eg}) \rangle \\
& + d_{fe'} d_{fe}^* d_{e'g} d_{eg}^* \times \langle E^\dagger(+z_{fe'} - z_{ff}) E(-z_{ee'} + z_{fe'}) E^\dagger(z_{eg} - z_{ee'}) E(z_{eg}) \rangle \\
& + d_{fe''} d_{fe'}^* d_{e'g} d_{eg}^* \times \langle E^\dagger(-z_{e''f} + z_{ff}) E(z_p - z_{e''f}) \sum_p \chi_{e''p}^R D_{pp}^{-1} E^\dagger(z_{ee'} - z_p) \chi_{pe}^L E(z_{eg}) \rangle \\
& \left. + d_{fe''} d_{fe'}^* d_{e'g} d_{eg}^* \times \langle E^\dagger(-z_{ef} + z_{ff}) E(+z_{ee'} - z_{ef}) E^\dagger(z_{eg} - z_{ee'}) E(z_{eg}) \rangle \right) \Big] \quad (B4)
\end{aligned}$$

which is amenable to numerical simulation.

Appendix C: Entangled photon correlation function

Here we present the numerical simulation of the square of the joint spectral amplitude function, for typical parameter regime used in the main simulation.

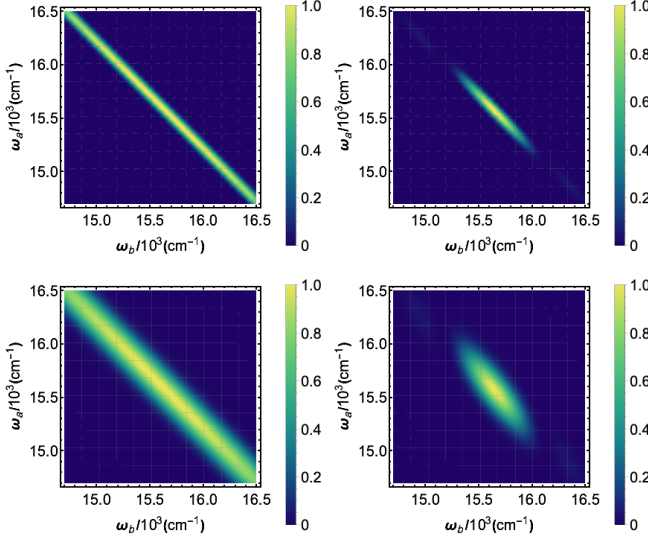


FIG. 8: The squared joint spectral amplitudes of the entangled photon pairs are displayed, illustrating variations in the entanglement time parameter (\tilde{T}_{ent}) and the temporal width of the SPDC pump (τ_0). They have noticeable implications for the nature of the frequency (anti-)correlations between the signal and idler pair, a feature that can be utilized for spectroscopic applications.

Appendix D: Temporal spectral filtering functions

We use the following temporal $F_{\bar{t}}(t)$, and spectral $F_{\bar{\omega}}(\omega)$ filtering functions, expressed as

$$F_{\bar{t}}(t') = \theta(t' - \bar{t}) \exp(-\sigma_{\bar{t}}(t' - \bar{t})) \quad (\text{D1})$$

$$F_{\bar{\omega}}(\omega') = i(\omega' - \bar{\omega} + i\sigma_{\omega})^{-1} \quad (\text{D2})$$

These functions have four tunable parameters: the centering variables, \bar{t} , $\bar{\omega}$, and the width $\sigma_{\bar{t}}$, $\sigma_{\bar{\omega}}$. The presented simulations in Fig. 7 illustrates their role in signal classification.

Appendix E: Note on the observable: photon coincidence signal

Here, we present a brief outline of derivation of the bare photon coincidence counting observable (i.e., without the filtering stage), following the original theory developed in [47, 48]. The expression is already presented in Eq. 11, and appears as

$$\begin{aligned} \langle N_s(t'_1, \tau_1) N_i(t'_2, \tau'_2) \rangle &= \int_{-\infty}^{t'_1} dt_1 \int_{-\infty}^{t'_1 + \tau_1} dt_3 \\ &\times \int_{-\infty}^{t'_2} dt_2 \int_{-\infty}^{t'_2 + \tau_2} dt_4 \langle V_R^\dagger(t_4) V_R^\dagger(t_3) V_L(t_1) V_L(t_2) \rangle \\ &\times \sum_{s,s'} \sum_{i,i'} \langle E_{s'R}(t_4) E_{i'R}(t_3) E_{s'R}^\dagger(t'_2 + \tau_2) E_{i'R}^\dagger(t'_1 + \tau_1) \\ &\times E_{iL}(t'_1) E_{sL}(t'_2) E_{iL}^\dagger(t_1) E_{sL}^\dagger(t_2) \rangle. \end{aligned} \quad (\text{E1})$$

Here, the averaging of the field correlation term is carried out over the detector modes, and the auxiliary photon modes, whereas the averaging of the exciton correlation term is carried out over two-exciton state following transport. In the presented theory, the leading order contributions to the signal arise from expansion of the time dependent density operator to the fourth order in emitted field. Assuming photon emission into vacuum modes, and following the standard algebraic manipulations one obtains

$$\begin{aligned} \langle N_s(t'_1, \tau_1) N_i(t'_2, \tau'_2) \rangle &= \mathcal{D}^2(\omega_1) \mathcal{D}^2(\omega_2) \\ &\times \langle V_R^\dagger(t'_2 + \tau_2) V_R^\dagger(t'_1 + \tau_1) V_L(t'_1) V_L(t'_2) \rangle. \end{aligned} \quad (\text{E2})$$

This expression represents the exciton correlation function weighted by the density of detector modes. The correlation function can be further expanded in terms of individual pathways Fig. 2, yielding the expressions in Eq. 19.

[1] H.-G. Duan, A. Jha, L. Chen, V. Tiwari, R. J. Cogdell, K. Ashraf, V. I. Prokhorenko, M. Thorwart, and R. D. Miller, Quantum coherent energy transport in the fenna–matthews–olson complex at low temperature, *Proceedings of the National Academy of Sciences* **119**, e2212630119 (2022).

[2] D. Abramavicius, B. Palmieri, and S. Mukamel, Extracting single and two-exciton couplings in photosynthetic complexes by coherent two-dimensional electronic spectra, *Chemical physics* **357**, 79 (2009).

[3] N. Lorenzoni, T. Lacroix, J. Lim, D. Tamascelli, S. F. Huelga, and M. B. Plenio, Full microscopic simulations uncover persistent quantum effects in primary photosynthesis, *Science Advances* **11**, eady6751 (2025).

[4] F. C. Spano, V. Agranovich, and S. Mukamel, Biexciton states and two-photon absorption in molecular monolayers, *The Journal of chemical physics* **95**, 1400 (1991).

[5] F. C. Spano and S. Mukamel, Cooperative nonlinear optical response of molecular aggregates: crossover to bulk behavior, *Physical review letters* **66**, 1197 (1991).

[6] E. Gutiérrez-Meza, R. Malatesta, H. Li, I. Bargigia, A. R. Srimath Kandada, D. A. Valverde-Chávez, S.-M. Kim, H. Li, N. Stingelin, S. Tretiak, *et al.*, Frenkel biexcitons in hybrid hj photophysical aggregates, *Science Advances* **7**, eabi5197 (2021).

[7] J. Dostál, F. Fennel, F. Koch, S. Herbst, F. Würthner, and T. Brixner, Direct observation of exciton–exciton interactions, *Nature communications* **9**, 1 (2018).

[8] S. Mueller and T. Brixner, Molecular coherent three-quantum two-dimensional fluorescence spectroscopy, *The Journal of Physical Chemistry Letters* **11**, 5139 (2020).

[9] Y. You, X.-X. Zhang, T. C. Berkelbach, M. S. Hybertsen, D. R. Reichman, and T. F. Heinz, Observation of biexcitons in monolayer wse2, *Nature Physics* **11**, 477 (2015).

[10] G. Soavi, S. Dal Conte, C. Manzoni, D. Viola, A. Narita, Y. Hu, X. Feng, U. Hohenester, E. Molinari, D. Prezzi, *et al.*, Exciton–exciton annihilation and biexciton stimulated emission in graphene nanoribbons, *Nature communications* **7**, 1 (2016).

[11] A. Debnath, C. Meier, B. Chatel, and T. Amand, High-fidelity biexciton generation in quantum dots by chirped laser pulses, *Physical Review B* **88**, 201305 (2013).

[12] Y.-a. Yan and O. Kühn, Laser control of dissipative two-exciton dynamics in molecular aggregates, *New Journal of Physics* **14**, 105004 (2012).

[13] O. Kühn, V. Chernyak, and S. Mukamel, Two-exciton spectroscopy of photosynthetic antenna complexes: Collective oscillator analysis, *The Journal of chemical physics* **105**, 8586 (1996).

[14] M. Kizmann, H. K. Yadalam, V. Y. Chernyak, and S. Mukamel, Quantum interferometry and pathway selectivity in the nonlinear response of photosynthetic excitons, *Proceedings of the National Academy of Sciences* **120**, e2304737120 (2023).

[15] P. Malý, J. Lüttig, P. A. Rose, A. Turkin, C. Lambert, J. J. Krich, and T. Brixner, Separating single-from multiparticle dynamics in nonlinear spectroscopy, *Nature* **616**, 280 (2023).

[16] M. Schröter, T. Pullerits, and O. Kühn, Using fluorescence detected two-dimensional spectroscopy to investigate initial exciton delocalization between coupled chromophores, *The Journal of Chemical Physics* **149** (2018).

[17] K. Hyeon-Deuk, Y. Tanimura, and M. Cho, Ultrafast exciton transfers in dna and its nonlinear optical spectroscopy, *The Journal of Chemical Physics* **128** (2008).

[18] M. R. Salvador, P. S. Nair, M. Cho, and G. D. Scholes, Interaction between excitons determines the non-linear response of nanocrystals, *Chemical Physics* **350**, 56 (2008).

[19] H. Lee, S. Cheon, and M. Cho, Chiroptical nature of two-exciton states of light-harvesting complex: Doubly resonant three-wave-mixing spectroscopy, *The Journal of chemical physics* **132** (2010).

[20] M. Cho, H. M. Vaswani, T. Brixner, J. Stenger, and G. R. Fleming, Exciton analysis in 2d electronic spectroscopy (2005).

[21] F. Schlawin, K. E. Dorfman, B. P. Fingerhut, and S. Mukamel, Suppression of population transport and control of exciton distributions by entangled photons, *Nature communications* **4**, 1 (2013).

[22] J. Javanainen and P. L. Gould, Linear intensity dependence of a two-photon transition rate, *Physical Review A* **41**, 5088 (1990).

[23] B. E. Saleh, B. M. Jost, H.-B. Fei, and M. C. Teich, Entangled-photon virtual-state spectroscopy, *Physical review letters* **80**, 3483 (1998).

[24] J. Peřina, B. E. Saleh, M. C. Teich, *et al.*, Multiphoton absorption cross section and virtual-state spectroscopy for the entangled n -photon state, *Physical Review A* **57**, 3972 (1998).

[25] K. E. Dorfman, F. Schlawin, and S. Mukamel, Nonlinear optical signals and spectroscopy with quantum light, *Reviews of Modern Physics* **88**, 045008 (2016).

[26] A. Ishizaki, Probing excited-state dynamics with quantum entangled photons: Correspondence to coherent multidimensional spectroscopy, *The Journal of Chemical Physics* **153** (2020).

[27] A. Debnath and A. Rubio, Entangled photon assisted multidimensional nonlinear optics of exciton–polaritons, *Journal of Applied Physics* **128**, 113102 (2020).

[28] Y. Fujihashi and A. Ishizaki, Achieving two-dimensional optical spectroscopy with temporal and spectral resolution using quantum entangled three photons, *The Journal of Chemical Physics* **155** (2021).

[29] Y. Fujihashi, K. Miwa, M. Higashi, and A. Ishizaki, Probing exciton dynamics with spectral selectivity through the use of quantum entangled photons, *The Journal of Chemical Physics* **159** (2023).

[30] Y. Fujihashi, A. Ishizaki, and R. Shimizu, Pathway selectivity in time-resolved spectroscopy using two-photon coincidence counting with quantum entangled photons, *The Journal of Chemical Physics* **160** (2024).

[31] M. G. Raymer, A. H. Marcus, J. R. Widom, and D. L. Vitullo, Entangled photon-pair two-dimensional fluorescence spectroscopy (epp-2dfs), *The Journal of Physical Chemistry B* **117**, 15559 (2013).

[32] O. Varnavski, S. K. Giri, T.-M. Chiang, C. J. Zeman IV, G. C. Schatz, and T. Goodson III, Colors of entangled two-photon absorption, *Proceedings of the National Academy of Sciences* **120**, e2307719120 (2023).

[33] R. Malatesta, L. Ubaldi, E. J. Kumar, E. Rojas-Gatjens, L. Moretti, A. Cruz, V. Menon, G. Cerullo, and A. R. S. Kandada, Optical microcavities as platforms for entangled photon spectroscopy, *arXiv preprint arXiv:2309.04751* (2023).

[34] M. Cho, Quantum optical measurement with tripartite entangled photons generated by triple parametric down-conversion, *The Journal of Chemical Physics* **148** (2018).

[35] Á. Martínez-Tapia, S. Corona-Aquino, F. Triana-Arango, C. You, R.-B. Jin, O. S. Magaña-Loaiza, S.-H. Dong, A. B. U'Ren, and R. d. J. León-Montiel, Witnessing entangled two-photon absorption via quantum interferometry, *APL Photonics* **8** (2023).

[36] M. G. Raymer and T. Landes, Theory of two-photon absorption with broadband squeezed vacuum, *Physical Review A* **106**, 013717 (2022).

[37] T. Landes, B. J. Smith, and M. G. Raymer, Limitations in fluorescence-detected entangled two-photon-

absorption experiments: Exploring the low-to high-gain squeezing regimes, *Physical Review A* **110**, 033708 (2024).

[38] T. Landes, M. G. Raymer, M. Allgaier, S. Merkouche, B. J. Smith, and A. H. Marcus, Quantifying the enhancement of two-photon absorption due to spectral-temporal entanglement, *Optics Express* **29**, 20022 (2021).

[39] K. M. Parzuchowski, A. Mikhaylov, M. D. Mazurek, R. N. Wilson, D. J. Lum, T. Gerrits, C. H. Camp Jr, M. J. Stevens, and R. Jimenez, Setting bounds on entangled two-photon absorption cross sections in common fluorophores, *Physical Review Applied* **15**, 044012 (2021).

[40] M. G. Raymer, T. Landes, M. Allgaier, S. Merkouche, B. J. Smith, and A. H. Marcus, How large is the quantum enhancement of two-photon absorption by time-frequency entanglement of photon pairs?, *Optica* **8**, 757 (2021).

[41] A. Khan, F. Albarelli, and A. Datta, Does entanglement enhance single-molecule pulsed biphoton spectroscopy?, *Quantum Science and Technology* **9**, 035004 (2024).

[42] F. Albarelli, E. Bisketzi, A. Khan, and A. Datta, Fundamental limits of pulsed quantum light spectroscopy: Dipole moment estimation, *Physical Review A* **107**, 062601 (2023).

[43] S. Das, A. Khan, F. Albarelli, and A. Datta, Optimal quantum spectroscopy using single-photon pulses, *arXiv preprint arXiv:2510.08386* (2025).

[44] K. E. Dorfman, S. Asban, L. Ye, J. R. Rouxel, D. Cho, and S. Mukamel, Monitoring spontaneous charge-density fluctuations by single-molecule diffraction of quantum light, *The journal of physical chemistry letters* **10**, 768 (2019).

[45] G. Lubin, D. Oron, U. Rossman, R. Tenne, and V. J. Yallapragada, Photon correlations in spectroscopy and microscopy, *ACS photonics* **9**, 2891 (2022).

[46] R. Pandya, P. Cameron, C. Vernière, B. Courme, S. Ithurria, A. Chin, E. Lhuillier, and H. Defienne, Towards robust detection of entangled two-photon absorption, *arXiv preprint arXiv:2410.06199* (2024).

[47] K. E. Dorfman and S. Mukamel, Nonlinear spectroscopy with time-and frequency-gated photon counting: A superoperator diagrammatic approach, *Physical Review A—Atomic, Molecular, and Optical Physics* **86**, 013810 (2012).

[48] K. E. Dorfman and S. Mukamel, Time-and-frequency-gated photon coincidence counting; a novel multidimensional spectroscopy tool, *Physica Scripta* **91**, 083004 (2016).

[49] D. Abramavicius, B. Palmieri, D. V. Voronine, F. Sanda, and S. Mukamel, Coherent multidimensional optical spectroscopy of excitons in molecular aggregates; quasiparticle versus supermolecule perspectives, *Chemical reviews* **109**, 2350 (2009).

[50] F. Schlawin, K. E. Dorfman, and S. Mukamel, Entangled two-photon absorption spectroscopy, *Accounts of chemical research* **51**, 2207 (2018).

[51] K. E. Dorfman and S. Mukamel, Multidimensional spectroscopy with entangled light: loop vs ladder delay scanning protocols, *New journal of physics* **16**, 033013 (2014).

[52] A. Debnath and A. Rubio, Entangled biphoton enhanced double quantum coherence signal as a probe for cavity polariton correlations in presence of phonon induced dephasing, *Frontiers in Physics* **10**, 879113 (2022).

[53] S. Mukamel and M. Richter, Multidimensional phase-sensitive single-molecule spectroscopy with time-and-frequency-gated fluorescence detection, *Physical Review A* **83**, 013815 (2011).

[54] S. Mukamel, Superoperator representation of nonlinear response: Unifying quantum field and mode coupling theories, *Physical Review E* **68**, 021111 (2003).